Statistical Narrow Band model for vibrational nonequilibrium CO2 radiation

Guillaume Janodet, Philippe Rivière, Jean-Michel Lamet, Valérie Rialland, Lionel Tessé, Anouar Soufiani

To cite this version:

Guillaume Janodet, Philippe Rivière, Jean-Michel Lamet, Valérie Rialland, Lionel Tessé, et al.. Statistical Narrow Band model for vibrational nonequilibrium CO2 radiation. Journal of Quantitative Spectroscopy and Radiative Transfer, 2024, 314, pp.108856. 10.1016/j.jqsrt.2023.108856 . hal-04220093v1

HAL Id: hal-04220093
https://hal.science/hal-04220093v1

Submitted on 27 Sep 2023 (v1), last revised 8 Dec 2023 (v2)

Statistical Narrow Band model for vibrational nonequilibrium CO_2 radiation

Guillaume Janodet[a,b,c], Philippe Rivière[a,*], Jean-Michel Lamet[b], Valérie Rialland[c], Lionel Tessé[d], Anouar Soufiani[a]

[a]*Laboratoire EM2C, CNRS, CentraleSupélec, Université Paris Saclay, 3 rue Joliot Curie, 91192 Gif-sur-Yvette Cedex, France*
[b]*ONERA/DMPE, Université de Toulouse, F-31055, Toulouse, France*
[c]*ONERA/DOTA, Université Paris-Saclay, BP80100, 91123 Palaiseau Cedex, France*
[d]*ONERA/DMPE, Université Paris-Saclay, F-92322, Châtillon, France*

Abstract

This paper presents the development of a Statistical Narrow Band (SNB) model for CO_2 in a nonequilibrium vibrational state. The population densities of the energy levels are modeled by a three-temperature approach (T, T_{12}, T_3) associated resp. to translation-rotation modes, symmetric-stretching and bending modes, and antisymmetric stretching mode, to compute nonequilibrium line by line (LBL) spectra. The nonequilibrium between vibrational temperatures induces spectral correlation issues between $\eta_\sigma/\kappa_\sigma$ and κ_σ, where η_σ and κ_σ are the emission and absorption coefficients respectively. To overcome this issue, a vibrational splitting of the spectroscopic database is made to separate lines with completely different vibrational transitions. The SNB parameters are obtained by fitting the curves of growth from the LBL approach by a least squares error minimization using a Newton method for pure Lorentz and Doppler broadening regimes for each line class. The total SNB

---

[*] Corresponding author.
Email address: `philippe.riviere@centralesupelec.fr` (Philippe Rivière)

Preprint submitted to JQSRT *September 25, 2023*

transmissivity is obtained by computing the product of each line class transmissivity, and the decorrelation between the spectra of the different classes is checked. Finally, the model is tested in Voigt broadening regime using a mixing rule by computing outlet radiative intensity of uniform and non-uniform columns and agrees well with the LBL approach. SNB parameters are available under request to the corresponding author.

Keywords: CO_2 radiation, Vibrational nonequilibrium, SNB model

---

1. Introduction

The Local Thermodynamic Equilibrium (LTE) assumption is no longer valid when internal relaxation time scales become comparable or higher than hydrodynamic time scales in gas flows. The gas is then under the Non-Local Thermodynamic Equilibrium (NLTE) state, which means that it contains an excess or a lack of internal energy compared to translational energy or even a non-Boltzmannian distribution of the populations of the different vibrational levels. This nonequilibrium aspect is found, for instance, in atmospheric entry flows [1, 2], electrically excited or gas dynamic CO_2 lasers [3, 4], or expanding flows like rocket plumes at high altitudes [5]. This departure from LTE affects the radiative properties of the radiating species and thus needs to be considered for radiative transfer.

One of the challenges in studying the radiation of gases under NLTE conditions is the knowledge of the population of each rovibrational energy level. The detailed vibrational state-to-state approach [6] is a priori the most accurate model for predicting level population densities. However, the total number of vibrational states of CO_2 with energies lower than the dissociation limit is estimated to be of the order of 10^5 [7]. Although some models attempt to bin vibrational levels based on physical arguments in order to reduce the computational complexity (see e.g., [7, 8]), the vibrational state-to-state approach remains impracticable in the context of radiative transfer calculations for coupled simulations in complex geometries. Moreover, the uncertainty about the kinetic rate constants of high-energy levels makes using the state-to-state approach very difficult. Therefore, the multi-temperature description of the thermodynamic state of CO_2, based on previous works [9, 10], is adopted in this study to compute vibrational level populations.

Once the spatial distributions of population densities are known, line-by-line (LBL) local absorption and emission spectra can be computed using suitable spectroscopic databases such as HITRAN [11], HITEMP [12] or CDSD-4000 [13] for CO_2 at high temperature. Such LBL calculations have been recently undertaken by Binauld et al. [9] to evaluate the effects of vibrational CO_2 NLTE on the infrared radiation emitted by an expanding flow in a conical nozzle or by high-altitude rocket plumes. It was shown in this study that the partial freeze of CO_2 vibration excitation, due to the strong expansion of the flow in the low-pressure atmosphere, may significantly increase the emission by the plume compared to the emission predicted from a single translation temperature. However, the LBL calculations were limited to some chosen lines of sight in the plume and 1D radiation calculations in the case of the nozzle flow. As for the state-to-state kinetic approach, the detailed LBL calculations also remain impracticable when the radiative transfer is to be coupled to flow-field calculations. Indeed, spectral, angular, and spatial integrations would require huge CPU time and storage capabilities. The development of accurate spectral band models is then highly desirable in this perspective.

In the framework of radiative transfer spectral modelling in nonequilibrium reentry flows, k-distribution models were first developed by Bansal et al. for N and O atomic radiation [14, 15] and then extended by Bansal et al. [16] to diatomic molecular species (N_2, N_2^+, NO, and O_2). Several spectral wide-band binning strategies and reduced order models have been compared in [17] for different reentry conditions. However, in the present work, global and wide-band models are excluded since one of the goals of the present study is to develop models suitable for spectrally integrated radiative transfer calculations and also for infrared signature simulations, which are limited to narrow spectral bands.

Among narrow-band models, k-distribution, with or without an extension with fictitious gases [18], remains challenging to apply in the case of reacting media with spatial change of chemical composition and strong pressure gradients. Statistical narrow-band models have been applied by Lamet et al. [19] for the prediction of radiative transfer in earth reentry flows and show a good ability to deal with diatomic molecules with the imbalance between electronic/vibration and translation/rotation (two-temperature description of the medium).

It is worth noticing that all NLTE radiation models mentioned above were dedicated to atomic or diatomic radiation, and none of them has considered polyatomic molecules like CO_2, where a disequilibrium may exist between the different vibration modes. Specific models have been developed for NLTE CO_2 radiation in [20]. However, the smeared band model was employed to get tractable simulations, which may fail for low-pressure applications with well-separated non-optically thin rotational lines. Another approach was developed first by Kudryavtsev and Novikov [21], and then by Vitkin et al. [22, 23], on the basis of statistical narrow-band mixing of lines belonging to different vibrational transitions. However, instead of using accurate spectroscopic databases, semi-analytical simplified models were employed to represent the spectral structure of CO_2 bands in the 4.3 and 2.7 μm regions. This approach was followed by Molchanov et al. [24] who used k-distribution method to compute partial transmissivities in the narrow bands.

This paper aims to develop a three-temperature SNB model for CO_2, considering spectral correlations and disequilibrium between vibrational modes (Section 2). CO_2 translational and rotational modes are assumed to be at local equilibrium and are described by a single temperature T due to the fast translation-rotation exchanges. Vibrational levels are assumed to follow a Boltzmann distribution at a single temperature T_{12} for the symmetric stretching mode, and the two-fold degenerate bending mode due to Fermi Resonance [25] and a Boltzmann distribution at a different temperature T_3 for the antisymmetric stretching mode. The model is then applied in Section 3 to a simple expanding supersonic nozzle flow and to radiative transfer along selected lines of sight in the high altitude plume of a solid propellant rocket as in [9]. The model accuracy is assessed through comparisons with line-by-line calculations.

2. SNB formulation

2.1. Radiative properties and multi-temperature model

The emission and absorption coefficients for wavenumber σ can be expressed under the assumption of independent lines as:

$$\eta_\sigma = \sum_{u-l} n_u \frac{A_{ul}}{4\pi} hc\sigma_{ul} f_{ul}(\sigma - \sigma_{ul}), \tag{1}$$

$$\kappa_\sigma = \sum_{u-l} (n_l B_{lu} - n_u B_{ul}) h\sigma_{ul} f_{ul}(\sigma - \sigma_{ul}), \tag{2}$$

where n_u and n_l are the populations of levels u and l, A_{ul}, B_{ul} and B_{lu} are the Einstein coefficients for spontaneous emission, induced emission, and absorption, σ_{ul} is the central wavenumber, and $f_{ul}(\sigma - \sigma_{ul})$ is the spectral line profile (assumed to be the same for the three radiative mechanisms) of the transition $u - l$. Spectroscopic data for CO_2 (Einstein coefficients, level energies, line positions, collisional broadening parameters) have been taken from the HITEMP-2010 [12] compilation, which has been recommended for applications up to 2000 K [13]. The population of any rovibrational level k of CO_2 in the multi-temperature approach of [9] can be expressed as follows:

$$n_k = n_{CO_2} Ab_I \frac{g_k}{Z_I(T,T_{12},T_3)} \exp\left(-\frac{E^{rot}\{k\}}{k_B T} - \frac{E^{\nu_{12}}\{k\}}{k_B T_{12}} - \frac{E^{\nu_3}\{k\}}{k_B T_3}\right), \tag{3}$$

where n_{CO_2} is the total population density of CO_2, Ab_I is the abundance of the considered isotopologue I, g_k is the degeneracy of the level k. The partitioning scheme of the energy is composed of a rotational part $E^{rot}\{k\}$, a vibrational part $E^{\nu_{12}}\{k\}$ associated with the coupled symmetric stretching-bending modes (ν_1,ν_2) and a vibrational part $E^{\nu_3}\{k\}$ corresponding to the asymmetric stretching mode ν_3. For each rovibrational level, these energies are calculated from the spectroscopic database according to

$$E^{rot}\{\mathrm{v}_1,l_2,\mathrm{v}_3,r,p,J\} = E\{\mathrm{v}_1,l_2,\mathrm{v}_3,r,p,J\} - \min_{J'} E\{\mathrm{v}_1,l_2,\mathrm{v}_3,r,p,J'\}, \quad (4)$$

$$E^{\nu_3}\{\mathrm{v}_1,l_2,\mathrm{v}_3,r,p,J\} = \min_{J'} E\{0,0,\mathrm{v}_3,1,e,J'\}, \quad (5)$$

$$E^{\nu_{12}}\{\mathrm{v}_1,l_2,\mathrm{v}_3,r,p,J\} = \min_{J'} E\{\mathrm{v}_1,l_2,\mathrm{v}_3,r,p,J'\} - E^{\nu_3}\{\mathrm{v}_1,l_2,\mathrm{v}_3,r,p,J\}, \quad (6)$$

where (v_1, l_2, v_3, r, p, J) are the quantum numbers used in HITEMP-2010 to identify the rovibrational levels k. v_1 and v_3 are quantum numbers associated respectively with the vibrational modes ν_1 and ν_3; l_2 is associated with the vibrational angular momentum of mode ν_2; the triplet (v_1, l_2, v_3) enables to identify the Fermi polyad to which the level k belongs; r is the index of the vibrational level associated to the level k among the $\mathrm{v}_1 + 1$ vibrational levels constituting the Fermi polyad, p is the parity (e or f) and J is the total angular momentum quantum number excluding nuclear spin of the level k. The populations of the few non-identified levels (0.9% of the lines see Table 2) have been calculated assuming LTE at temperature T. $Z_I(T, T_{12}, T_3)$ in Eq.(3) is the three-temperature partition function of the isotopologue I, which has been calculated using the approximation of the three uncoupled harmonic oscillators associated with the vibrational modes of CO_2 and the rigid rotor and is given by:

$$Z_I(T,T_{12},T_3) = \frac{k_b T}{\alpha_I B_I} \times \frac{1}{1-\exp(-\omega_{1I}/k_b T_{12})} \frac{1}{[1-\exp(-\omega_{2I}/k_b T_{12})]^2} \frac{1}{1-\exp(-\omega_{3I}/k_b T_3)} \quad (7)$$

broadening regime	resolution [cm^{-1}]	line wing cut-off [cm^{-1}]	spectral domain [cm^{-1}]
Lorentz	10^{-2}	50	[237.5, 8312.5]
Doppler	10^{-3}	10	[237.5, 8312.5]
Voigt	10^{-3}	50	[237.5, 8312.5]

Table 1: Input parameters for the LBL calculations

where B_I is the rotational constant of isotopologue I, $\alpha_I = 1$ or 2 depending on the isotopologue symmetry, ω_{1I}, ω_{2I} and ω_{3I} are the vibration energies associated with the three fundamental vibration modes taken for the different isotopologues from [26].

The models and data presented here are used to perform LBL calculations for building vibrational nonequilibrium SNB models for CO_2 in Doppler, and Lorentz broadening regimes. The Voigt broadening regime will be recovered using a mixing approach (see below), whose validation will also require LBL calculations in the Voigt regime. In the following, all calculations were achieved for a CO_2-N_2 mixture with a molar fraction $x_{CO_2} = 0.5$ using the input parameters provided in Table 1.

2.2. Spectral correlation issues

The radiative transfer equation (RTE) along a line of sight in nonscattering media is given by

$$\frac{dI_\sigma(s)}{ds} = \eta_\sigma(s) - \kappa_\sigma(s) I_\sigma(s), \tag{8}$$

where $I_\sigma(s)$ is the radiative intensity at the abscissa s along the line of sight. The absorption and emission coefficients must be calculated beforehand to solve this equation. This section aims to develop an RTE formulation under nonequilibrium conditions suitable for applying statistical narrow-band models. From Eq.(8), we can express the intensity escaping from a column $(0,s)$ at s as:

$$I_\sigma(s) = \int_0^s \eta_\sigma(s')\tau_\sigma(s',s)\; ds', \tag{9}$$

where $\tau_\sigma(s',s) = \exp(-\int_{s'}^{s} \kappa_\sigma(s'')ds'')$ is the transmissivity of the column (s',s) and $I_\sigma(s=0)$ is assumed equal to 0.

To use SNB models for solving the RTE, we must express the intensity averaged over the spectral band $\Delta\sigma$. However, the emission coefficient η_σ and the transmissivity τ_σ are strongly correlated. To correctly account for self-correlation, the intensity averaged over the spectral band $\Delta\sigma$ is expressed as

$$\overline{I_\sigma}^{\Delta\sigma}(s) = \int_0^s \overline{\frac{\eta_\sigma}{\kappa_\sigma}(s')\frac{\partial\tau_\sigma}{\partial s'}(s',s)}^{\Delta\sigma}\; ds'. \tag{10}$$

To compute Eq. (10) with SNB models, a further simplification is necessary, which is

$$\overline{I_\sigma}^{\Delta\sigma}(s) \approx \int_0^s \overline{\left(\frac{\eta_\sigma}{\kappa_\sigma}(s')\right)}^{\Delta\sigma} \frac{\partial\overline{\tau_\sigma}^{\Delta\sigma}}{\partial s'}(s',s)\; ds' \tag{11}$$

assuming that $\frac{\eta_\sigma}{\kappa_\sigma}$ and $\frac{\partial\tau_\sigma}{\partial s'}$ are not correlated. This assumption is valid in LTE conditions because the ratio $\frac{\eta_\sigma}{\kappa_\sigma}$ is equal to the Planck's function $I^0_\sigma(T)$. However, it is not guaranteed in NLTE conditions since Kirchhoff's law is no longer valid and the ratio $\frac{\eta_\sigma}{\kappa_\sigma}$ can present important spectral dynamics. The Fig.1 presents two nonequilibrium conditions: an imbalance between vibration and rotation (right) and an imbalance between the vibrational modes and the rotation (left). It is clear that the ratio follows neither

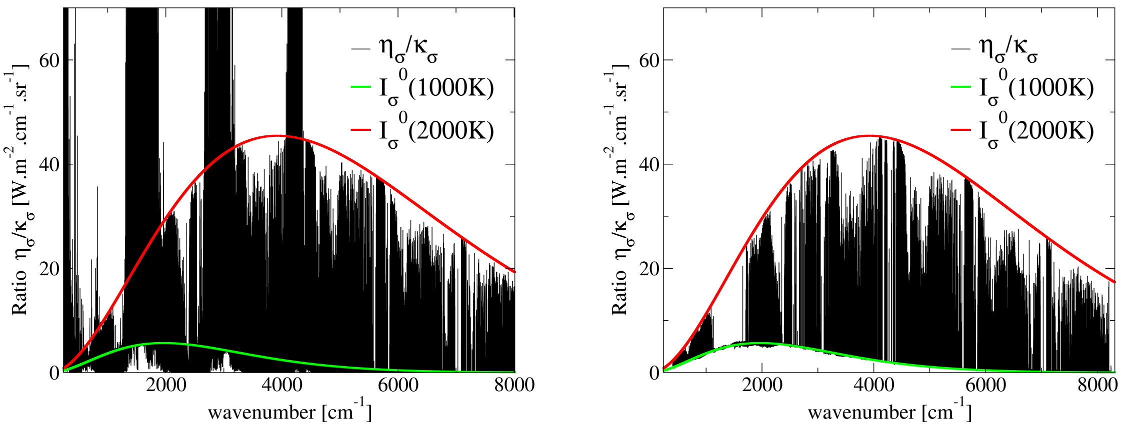

Figure 1: LBL $\eta_\sigma/\kappa_\sigma$ spectrum for $p = 1000$ Pa, $T = 2000$ K, $T_{12} = 1000$ K, $T_3 = 300$ K (left) and $p = 1000$ Pa, $T = 2000$ K, $T_{12} = 1000$ K, $T_3 = 1000$ K (right)

Planck's function at temperature T_{12} nor Planck's function at temperature T_3 as shown in Fig.1 (left). The spectral dynamics are then more important than for rotation-vibration nonequilibrium, as shown in Fig.1 (right) and in [19]. Comparing $\overline{\eta_\sigma}^{\Delta\sigma}$ to $\overline{\eta_\sigma/\kappa_\sigma}^{\Delta\sigma} \times \overline{\kappa_\sigma}^{\Delta\sigma}$ is the most critical test to check the decorrelation assumption. Indeed, the expression of the intensity averaged over the spectral band $\Delta\sigma$ exiting of uniform column of length l considering the decorrelation assumption is given by :

$$\overline{I_\sigma}^{\Delta\sigma}(0 \to l) = \int_0^l \overline{\left(\frac{\eta_\sigma}{\kappa_\sigma}\right)}^{\Delta\sigma} \frac{\partial \overline{\tau_\sigma}^{\Delta\sigma}}{\partial s'}(s',l)\, ds' = \overline{\left(\frac{\eta_\sigma}{\kappa_\sigma}\right)}^{\Delta\sigma} \left(1 - \overline{\tau_\sigma}^{\Delta\sigma}(0 \to l)\right). \tag{12}$$

The spectral dynamics of the emissivity $1 - \tau_\sigma(0 \to l)$ is maximum when the medium is optically thin because the exponential function does not smooth the absorption coefficient spectral structures. The expression of the radiative

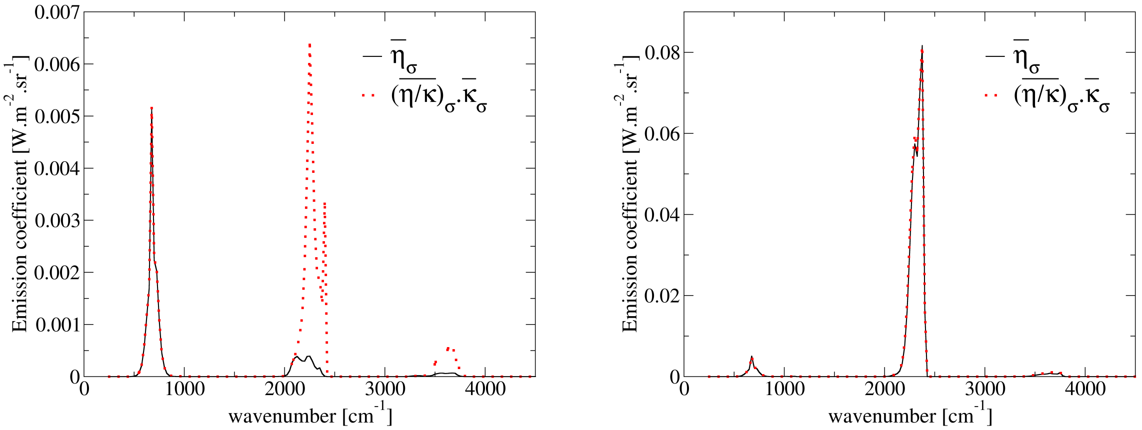

Figure 2: Comparison between $\overline{\eta_\sigma}^{\Delta\sigma}$ and $\overline{\eta_\sigma/\kappa_\sigma}^{\Delta\sigma} \times \overline{\kappa_\sigma}^{\Delta\sigma}$ for $p = 1000$ Pa, $T = 2000$ K, $T_{12} = 1000$ K, $T_3 = 300$ K (left) and $p = 1000$ Pa, $T = 2000$ K, $T_{12} = 1000$ K, $T_3 = 1000$ K (right)

intensity is, considering the decorrelation hypothesis, equal to

$$\overline{I_\sigma}^{\Delta\sigma}(0 \to l) \underset{\kappa_\sigma l \to 0}{=} \overline{\left(\frac{\eta_\sigma}{\kappa_\sigma}\right)}^{\Delta\sigma} \overline{\kappa_\sigma}^{\Delta\sigma} l, \tag{13}$$

which explains the choice of comparing $\overline{\eta_\sigma}^{\Delta\sigma}$, the exact result, to $\overline{\eta_\sigma/\kappa_\sigma}^{\Delta\sigma} \times \overline{\kappa_\sigma}^{\Delta\sigma}$ for verifying the decorrelation assumption. These tests were performed for realistic strong nonequilibrium conditions. It turns out that the decorrelation assumption between $\eta_\sigma/\kappa_\sigma$ and κ_σ is not valid for cases with a strong imbalance between the temperatures T_{12} and T_3 and a pressure $P \leq 10^4$ Pa, as shown in Fig. 2 (left). The influence of pressure on spectral dynamics is well known. Indeed, the line widths for Lorentz broadening regime are proportional to the pressure. Thus, decreasing the pressure increases the spectral dynamics and, therefore, the spectral correlation between $\eta_\sigma/\kappa_\sigma$ and κ_σ. Nevertheless, more than pressure's influence is needed to explain these spectral correlations since the decorrelation assumption is always verified at LTE. It combines being in both moderate pressure conditions and a strong imbalance between the two vibration temperatures. Fig. 2 (left) shows that the correlation issue arises only for the 2.7 μm and 4.3 μm bands. To understand further why these spectral bands are problematic under these conditions, high-resolution spectra of κ_σ and η_σ under the strong vibrational imbalance condition of Fig.2 (left part) have been plotted in Fig. 3 (lower and middle part of the figure), for a very narrow spectral range $[2247.62, 2247.69]$ cm^{-1} belonging to a problematic narrow-band identified in Fig.2. In the upper part of Fig. 3 are also plotted both $\eta_\sigma/\kappa_\sigma$ and again κ_σ, using a logarithmic scale, exhibiting a strong anticorrelation between κ_σ and $\eta_\sigma/\kappa_\sigma$: in this region, the absorption spectrum is dominated by vibrational transitions of the type $\Delta v_3 = 1$ near 2247.63 and 2247.675 cm^{-1} as mentioned in the lowest part of the figure; these transitions also contribute to the emission spectrum near the same spectral locations, but transitions of type ($\Delta v_1 = 1$, $\Delta l_2 = 1$) also contribute to the emission spectrum near 2247.655 cm^{-1} as indicated on the middle part of Fig. 3.[1] Each of these types of vibrational transitions, considered as an isolated line $(u - l)$, will be characterized by very different values of the ratio $(\eta_\sigma/\kappa_\sigma)_{ul}$, whose general expression is

$$\left(\frac{\eta_\sigma}{\kappa_\sigma}\right)_{ul} = \frac{2hc\sigma_{ul}^3}{\exp\left(\dfrac{\Delta E_{ul}^{\nu_{12}}}{k_B T_{12}} + \dfrac{\Delta E_{ul}^{\nu_3}}{k_B T_3} + \dfrac{\Delta E_{ul}^{rot}}{k_B T}\right) - 1}. \tag{14}$$

In the above equation, $\Delta E_{ul}^{\nu_{12}}$, $\Delta E_{ul}^{\nu_3}$, and ΔE_{ul}^{rot} designate the energy varia-

---

[1] Let note that about 16 rovibrational transitions are required to accurately model the spectra shown in Fig. 3: to simplify the analysis, only three dominant vibrational transitions have been mentioned near the local maximum of the spectra.

tion associated to resp. vibrational mode 12, vibrational mode 3, and rotation for the transition ul. For the two types of vibrational transitions identified above, resp. $\Delta v_3 = 1$ and ($\Delta v_1 = 1$, $\Delta l_2 = 1$), the transition energy $hc\sigma_{ul}$ is mainly defined resp. by $\Delta E_{ul}^{\nu_3}$ and $\Delta E_{ul}^{\nu_{12}}$, while the rotational contribution $\Delta E_{ul}^{rot}/(k_B T)$ inside the exponential in Eq. (14) is negligible in comparison with vibrational one at $T = 2000$ K; the associated ratios $(\eta_\sigma/\kappa_\sigma)_{ul}$ may be therefore approximated according to

$$\left(\frac{\eta_\sigma}{\kappa_\sigma}\right)_{\Delta v_3=1} \approx \frac{2hc\sigma_{ul}^3}{\exp\left(\dfrac{hc\sigma_{ul}}{k_B T_3}\right) - 1}, \tag{15}$$

$$\left(\frac{\eta_\sigma}{\kappa_\sigma}\right)_{\Delta v_1=1,\Delta l_2=1} \approx \frac{2hc\sigma_{ul}^3}{\exp\left(\dfrac{hc\sigma_{ul}}{k_B T_{12}}\right) - 1}, \tag{16}$$

and will be very different from each other in the condition ($T_3 = 300$ K, $T_{12} = 2000$ K) considered here. Although the overlapping between lines, especially at not too low pressures, should moderate this analysis (the absorption coefficient near 2247.655 cm^{-1} is dominated by the line wings of the transitions $\Delta v_3 = 1$ even at 1000 Pa), the variability of the $(\eta_\sigma/\kappa_\sigma)_{ul}$ values of the various contributing transitions to emission or absorption spectra explains the anticorrelation between κ_σ and $\eta_\sigma/\kappa_\sigma$ observed in Fig. 3, and thus the overestimation of the emission observed in Fig.2 (left) when using the decorrelation hypothesis Eq. 13. It is quite obvious from Eq. 14 that the variability of $(\eta_\sigma/\kappa_\sigma)_{ul}$ values will occur under strong vibrational disequilibrium among vibrational transitions of different nature, viz. characterised by very different vibrational energy variations ($\Delta E_{ul}^{\nu_3}$,$\Delta E_{ul}^{\nu_{12}}$). Grouping transitions into classes of similar vibrational energy variations will reduce the variability of $(\eta_\sigma/\kappa_\sigma)_{ul}$ inside each class and, therefore, improve the accuracy of the decorrelation approximation Eq. 13 when applied to the lines of a given class. Let note that the good behaviour of this decorrelation assumption in the 15 μm region (see Fig. 2) is consistent with the above analysis since in this spectral region, vibrational transitions involving only the mode (ν_1,ν_2) are dominant.

2.3. Definition of line classes

Considering that the fundamental vibrational energies of mode ν_1 and ν_2 approximately satisfy $\omega_{1I} \approx 2\omega_{2I}$ for each isotopologue I, the more accurate approach to ensure the decorrelation assumption's validity would consist of grouping the lines into classes according to the different observed values of $(2\Delta v_1 + \Delta l_2, \Delta v_3)$. Such an approach would lead to the introduction of more than 20 classes leading to a quite tedious model. Observing that in the two main spectral regions where CO$_2$ radiation has to be accounted for and where correlation issues arise, i.e. the 4.3 μm and the 2.7 μm regions, the main vibrational transitions satisfy $\Delta v_3 = 1$, it appears quite natural to split the database into lines satisfying $\Delta v_3 = 1$ or $\Delta v_3 \neq 1$. Table 2 presents the different line classes that have been defined and the distribution of the transitions per class.

name	$\nu3$	$not\_\nu3$	$not\_defined$
definition	$\Delta \mathrm{v}_3 = (\mathrm{v}_3)' - (\mathrm{v}_3)'' = 1$	$\Delta \mathrm{v}_3 \neq 1$	$r' = 0$ or $r'' = 0$
proportion of lines	4554364 (40.9%)	6482107 (58.2%)	99692 (0.9%)

Table 2: Line classes for CO$_2$

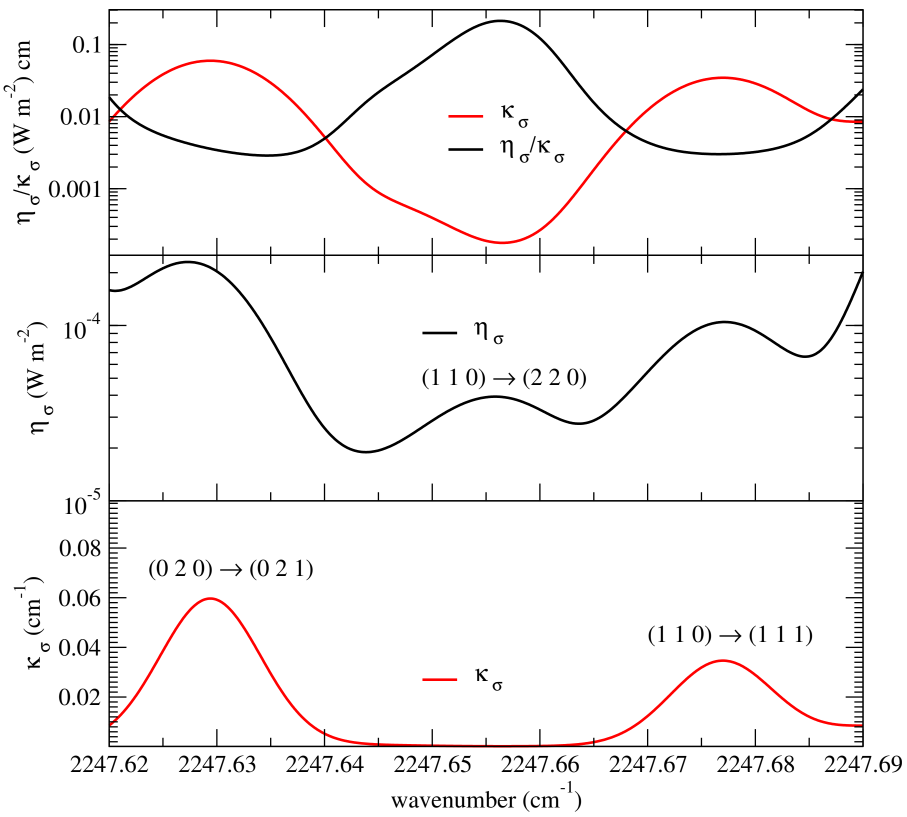

Figure 3: Absorption (κ_σ) and emission (η_σ) spectra of a CO_2-N_2 mixture at $T = 2000$ K, $T_{12} = 1000$ K, $T_3 = 300$ K, $p = 1000$ Pa. Typical dominant vibrational transitions (see footnote 1) are indicated near each local maximum of the spectra using the notation $(v_1 l_2 v_3)'' \rightarrow (v_1 l_2 v_3)'$ to designate lower $''$ and upper $'$ vibrational states. The upper part of the figure exhibits the anticorrelation between $\eta_\sigma/\kappa_\sigma$ and κ_σ for this strong vibrational imbalance condition.

The ν_3 and not_ν_3 classes represent more than 99% of the database lines. The class $not\_defined$ contains the lines for unknown upper or lower vibrational energy levels. It seems natural to consider these lines separately because we cannot use vibrational temperatures to predict the population of their asso-

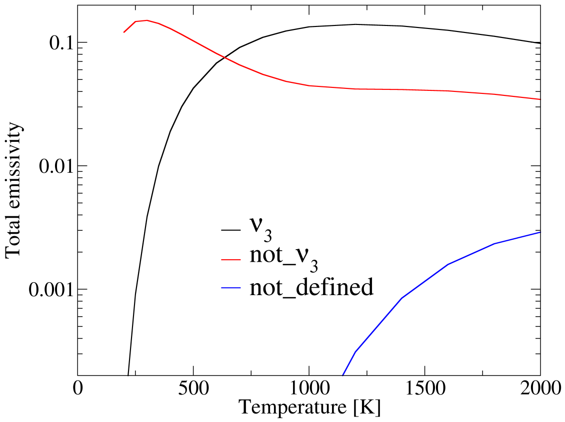

Figure 4: Comparison of emissivities of the three classes vs temperature at LTE for $p =$ 100000 Pa, $l = 1$ m and $x_{\mathrm{CO_2}} = 0.5$

ciated upper or lower levels; that is why these level populations are assumed to follow a Boltzmann distribution at the translation/rotation temperature T. To evaluate the contribution of each class to the gas radiative properties, a comparison of the total emissivity of each class as a temperature function (at LTE) is plotted in Fig. 4. The total emissivity is computed following

$$\epsilon_{tot,class}(x,p,l,T) = \frac{\pi}{\sigma_{SB} T^4} \sum_{bands\ \ b} \left(1 - \overline{\tau_b}^{\Delta\sigma}(x,p,l,T)\right) \overline{I_b^0}^{\Delta\sigma}(T)\Delta\sigma, \tag{17}$$

where σ_{SB} is the Stefan-Boltzmann constant and I^0 is Planck's function. The ν_3 class ($\Delta \mathrm{v}_3 = 1$) is the one that contributes the most above T=700 K, and the not_ν_3 class ($\Delta \mathrm{v}_3 \neq 1$) is dominant below. As expected, the contribution of the $not\_defined$ class is weak compared to the other classes.

Henceforth, a check for the validity of the decorrelation assumption is performed for each class. The one for the $not\_defined$ class is useless because

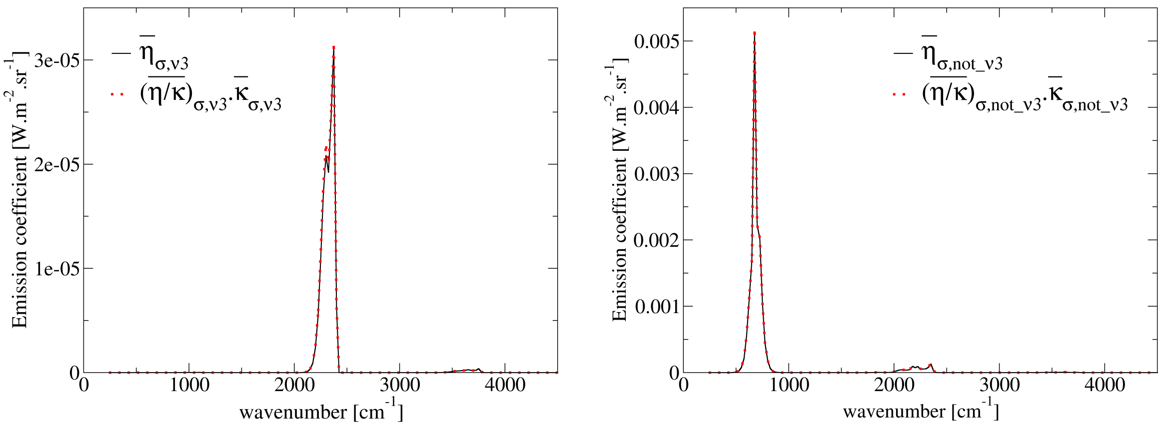

Figure 5: Emission coefficient for $\nu3$ class (left) and not_$\nu3$ class (right) for $p = 1000$ Pa, $T = 2000$ K, $T_{12} = 1000$ K and $T_3 = 300$ K

level populations for these lines are assumed at LTE. Fig.5 shows that splitting into line classes solves the spectral correlation issue between $\eta_\sigma/\kappa_\sigma$ and κ_σ. The formulation of the RTE equation, averaged over $\Delta\sigma$, with the multiclass approach for CO_2 is expressed following Lamet et al. [19], as :

$$\overline{I}_\sigma^{\Delta\sigma}(l) = \sum_{j=1}^{N_{class}} \int_0^l \overline{\left(\frac{\eta_\sigma}{\kappa_\sigma}\right)_j}^{\Delta\sigma}(s) \frac{\partial \overline{\tau_j}^{\Delta\sigma}}{\partial s}(s,l) \prod_{j'\neq j} \overline{\tau_{j'}}^{\Delta\sigma}(s,l)\; ds, \tag{18}$$

where a decorrelation assumption between classes has been used. The validity of this assumption is checked in Fig.6 and shows that the product of the transmissivities is indeed very close to the total transmissivity $\overline{\tau_\sigma}^{\Delta\sigma}$ of CO_2.

2.4. Statistical narrow band model parameters

Equation (18) shows that the model requires the computation of parameters $\overline{(\eta_\sigma/\kappa_\sigma)_j}^{\Delta\sigma}$ and of transmissivities. The parameters $\overline{(\eta_\sigma/\kappa_\sigma)_j}^{\Delta\sigma}$ were directly tabulated from LBL calculations, and were found to be insensitive to line

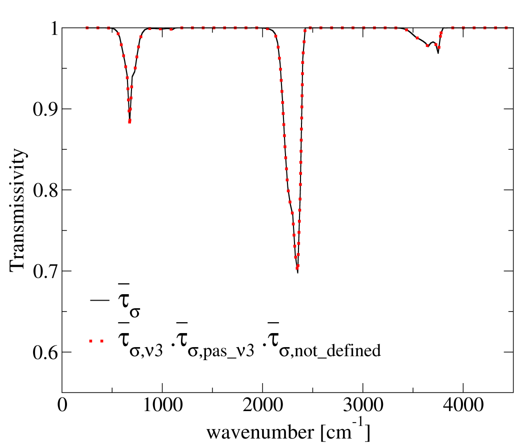

Figure 6: Comparison of the transmissivity product for each class with the total transmissivity

broadening regime. For transmissivities, the random SNB model of Mayer and Goody [27] has been selected in this study since it provides accurate results for polyatomic molecules at LTE. This model is based on statistical assumptions concerning line positions and intensities within a narrow band of width $\Delta\sigma$ and allows to express the transmissivity of a uniform column of length l, averaged over $\Delta\sigma$ as

$$\overline{\tau}^{\Delta\sigma}(l) = \frac{1}{\Delta\sigma}\int_{\Delta\sigma} \exp(-\kappa_\sigma l)d\sigma = \exp(-\frac{\overline{W}}{\delta}), \tag{19}$$

where $\delta = \Delta\sigma/N$ is the mean spacing between the N line positions within $\Delta\sigma$, and $\overline{W}$ is the mean black equivalent width of these lines, defined as

$$\overline{W} = \frac{1}{N}\sum_{r=1}^{N}\int_{-\infty}^{+\infty}[1-\exp(-\kappa_\sigma^r l)]d\sigma, \tag{20}$$

where κ_σ^r is the contribution of the r^{th} line to the absorption coefficient. Several line intensity distribution functions have been proposed to model

$\overline{W}/\delta$ for Lorentz and Doppler line broadening. The most used are the Goody exponential distribution [27], and the Malkmus tailed inverse-exponential distribution [28]. They are special cases (respectively for $\alpha = -1$ and $\alpha = 0$) of the generalized Malkmus distribution function of [29]. Its expression is the following

$$P_\alpha(S) : \frac{C_\alpha}{S}\left(\frac{S_m}{S}\right)^\alpha \left[\exp\left(-\frac{S}{S_m}\right) - \exp\left(-\frac{rS}{S_M}\right)\right], \tag{21}$$

where C_α is a normalization constant. In this study, the Malkmus distribution function is used for the Lorentz broadening regime leading to

$$\frac{\overline{W_L}}{\delta} = \frac{2\overline{\gamma_L}}{\overline{\delta_L}}\left(\sqrt{1 + \frac{\overline{k_L}xpl\overline{\delta_L}}{\overline{\gamma_L}}} - 1\right). \tag{22}$$

In the Doppler broadening regime, P_α distribution leads to the mean equivalent line width expression

$$\frac{\overline{W_D}}{\delta} = \overline{\beta_D} H_\alpha\left(\frac{\overline{k_D}xpl}{\overline{\beta_D}}\right) \tag{23}$$

with

$$H_\alpha(y) = \frac{1}{\alpha\sqrt{\pi}}\int_{-\infty}^{+\infty}[(1 + y\exp(-\xi^2))^\alpha - 1]d\xi \qquad \text{for } \alpha \neq 0 \tag{24}$$

$$H_0(y) = \frac{1}{\sqrt{\pi}}\int_{-\infty}^{+\infty}\ln[1 + y\exp(-\xi^2)]d\xi \qquad \text{for } \alpha = 0, \tag{25}$$

where $\overline{\delta_L}$ is a modified mean line spacing and $\overline{\beta_D}$ characterizes the degree of line overlapping. $\overline{k_{L/D}}$ is the reduced mean absorption coefficient and can be considered equal for the Lorentz and Doppler broadening regime ($\overline{k_L} = \overline{k_D} = \overline{k} = \overline{\kappa_\sigma}/(x_{\mathrm{CO_2}}p)$) with good accuracy. The parameter $\overline{\gamma_L}$ represents the mean Lorentz half width at half maximum of the lines and is expressed for $\mathrm{CO_2}$ as

[30]

$$\overline{\gamma_L} = \frac{p}{p_s}\left(\frac{T_s}{T}\right)^{0.7}\left[0.07x_{\mathrm{CO}_2} + 0.058\left(1 - x_{\mathrm{CO}_2}\right)\right], \tag{26}$$

where $p_s = 1$ atm and $T_s = 296$ K.

For each broadening regime and each line class, parameters $\overline{k}$ have been obtained directly by averaging over each narrow band ($\Delta\sigma = 25$ cm^{-1}) high-resolution absorption coefficients provided by LBL calculations based on the HITEMP-2010 database. The parameters $\overline{\delta_L}$ and $\overline{\beta_D}$ have been generated from adjustments enabling the corresponding analytical expression of $\overline{W_{L/D}/\delta}$, as a function of the column length l, to fit $-\ln(\overline{\tau}^{\Delta\sigma}(l))$ obtained with LBL calculations (called the curve of growth). This adjustment is made by minimizing the least square error thanks to the Newton method. The parameters $\overline{\delta_L}$ and $\overline{k}$ are assumed independent of the pressure and are generated at $p = 1$ bar. For the curve of growth adjustments in the Lorentz broadening regime, 20 transmissivities are prescribed from 0.02 to 0.95, and the associated column lengths are computed from these transmissivities. For the adjustments in Doppler broadening regime, 21 column lengths are provided from $x_{\mathrm{CO}_2}pl = 5$ Pa.m to $x_{\mathrm{CO}_2}pl = 5000$ Pa.m with a regular logarithmic step. Indeed, prescribing transmissivities near 0 for the Doppler broadening regime would lead to huge and unrealistic column lengths. The parameter α in the distribution function is equal to 0.3 excepted for narrow band centers $\sigma = 2350/2375/2400$ cm^{-1} where $\alpha = 0.2$. To quantify the errors introduced by the SNB model for uniform columns, a mean quadratic error is defined for the mean transmissivity $\overline{\tau}^{\Delta\sigma}$ as follows for each spectral band

$$s_\tau(\sigma) = \sqrt{\frac{1}{N_T.N_{T_{12}}.N_{T_3},N_l,N_{class}}} \times \sqrt{\left(\sum_{i=1}^{N_T}\sum_{j=1}^{N_{T_{12}}}\sum_{k=1}^{N_{T_3}}\sum_{l=1}^{N_l}\sum_{n=1}^{N_{class}} \left((\overline{\tau}^{\Delta\sigma}_{LBL} - \overline{\tau}^{\Delta\sigma}_{SNB})(\sigma,T_i,T_{12,j},T_{3,k},l_l,class_n)\right)^2\right)}, \tag{27}$$

and a relative mean quadratic error is defined for $1 - \overline{\tau}^{\Delta\sigma}$ for each spectral band according to

$$s_{rel,1-\tau}(\sigma) = \sqrt{\frac{1}{N_T.N_{T_{12}}.N_{T_3},N_l,N_{class}}} \times \sqrt{\left(\sum_{i=1}^{N_T}\sum_{j=1}^{N_{T_{12}}}\sum_{k=1}^{N_{T_3}}\sum_{l=1}^{N_l}\sum_{n=1}^{N_{class}} \left(\left(\frac{\overline{\tau}^{\Delta\sigma}_{LBL} - \overline{\tau}^{\Delta\sigma}_{SNB}}{1 - \overline{\tau}^{\Delta\sigma}_{LBL}}\right)(\sigma,T_i,T_{12,j},T_{3,k},l_l,class_n)\right)^2\right)}, \tag{28}$$

where $N_T, N_{T_{12}}, N_{T_3}, N_{class}$ are the number of grid points of the variables $T, T_{12}, T_3, class$, respectively, for which parameters have been obtained. For the temperatures, the grid contains the 32 following values: [200, 250, 300, 350, 400, 450, 500, 600, 700, 800, 900, 1000, 1100, 1200, 1300, 1400, 1500, 1600, 1700, 1800, 1900, 2000, 2200, 2400, 2600, 2800, 3000, 3200, 3400, 3600, 3800, 4000]. The N_l lengths l correspond to the ones used to perform the curve of growth adjustments of $\overline{\delta_L}$ and $\overline{\beta_D}$. These error estimators are presented in Fig. 7 and Fig. 8 and show that the adjustment errors are maximum when performed in the absorption bands, which is expected since the curves of growth are linear for small optical thicknesses. The errors for

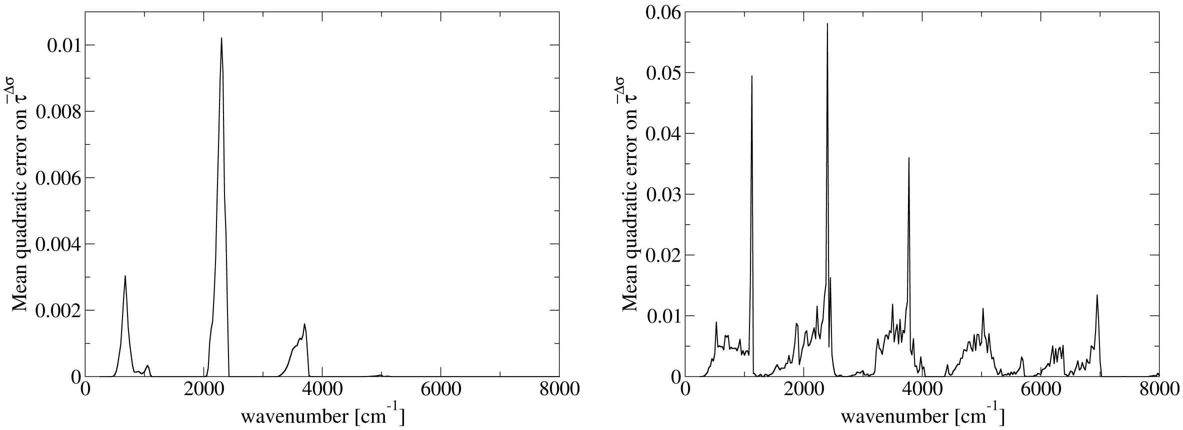

Figure 7: Mean quadratic error on $\overline{\tau}^{\Delta\sigma}$ for Doppler broadening regime (left) and Lorentz broadening regime (right)

Lorentz broadening regime appear higher than for the Doppler regime. However, transmissivities are prescribed in Lorentz broadening, which means that the adjustment is made for a wide range of optical thicknesses. Therefore, the errors displayed for Lorentz broadening involve contributions of all transmissivity ranges, unlike for Doppler broadening, where errors are checked on the optically thin or medium part of the curve of growth.

In the context of high-altitude rocket plumes, we have to consider the Voigt broadening regime for which the mean black equivalent line width is calculated by combining $\overline{W_L}/\delta$ and $\overline{W_D}/\delta$ expressions, according to the Ludwig formula

$$\frac{\overline{W_V}}{\delta} = \overline{k}xpl\sqrt{1-\Omega^{-1/2}} \quad \text{with}$$

$$\Omega = \left[1-\left(\frac{1}{\overline{k}xpl}\frac{\overline{W_D}}{\delta}\right)^2\right]^{-2} + \left[1-\left(\frac{1}{\overline{k}xpl}\frac{\overline{W_L}}{\delta}\right)^2\right]^{-2} - 1 \qquad (29)$$

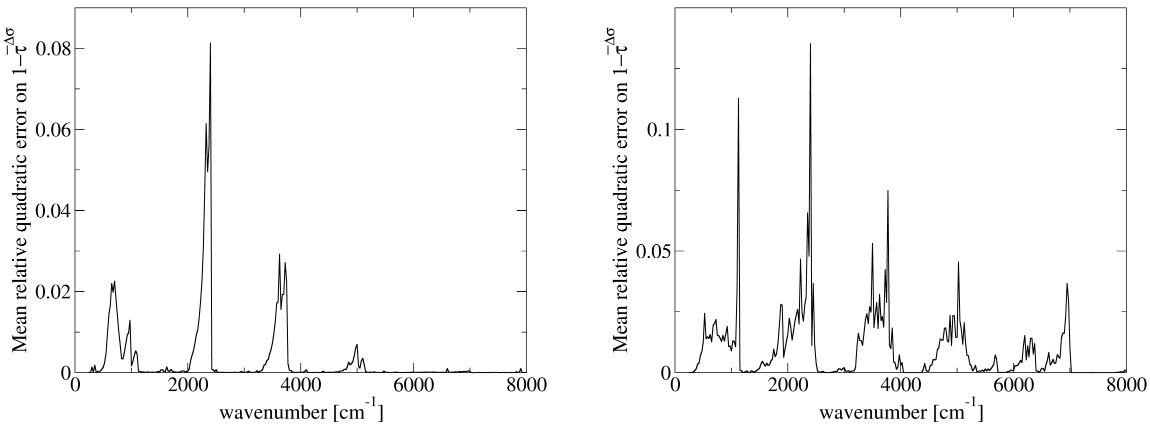

Figure 8: Mean relative quadratic error on $1 - \overline{\tau}^{\Delta\sigma}$ for Doppler broadening regime (left) and Lorentz broadening regime (right)

as proposed in [31].

To validate the SNB model in this regime, we compare the radiative intensity at the exit of a uniform column from the model expressed as Eq.(18) and the LBL approach for the nonequilibrium conditions considered in Fig. 2 in a wide range of pressure. This allows us to check the model in all broadening regimes and ensure that the mixing formula and the mixing of classes do not downgrade model accuracy. The comparison in Fig. 9 shows a good agreement between the SNB model and the LBL approach for the two conditions.

To conclude this subsection, the SNB parameters $\overline{(\eta_\sigma/\kappa_\sigma)}^{\Delta\sigma}$, $\overline{k}$, $\overline{\delta_L}$, and $\overline{\beta_D}$ have been tabulated as function of the three temperatures T, T_{12}, and T_3, for each class and each narrow band.The temperature grid is the one given above.

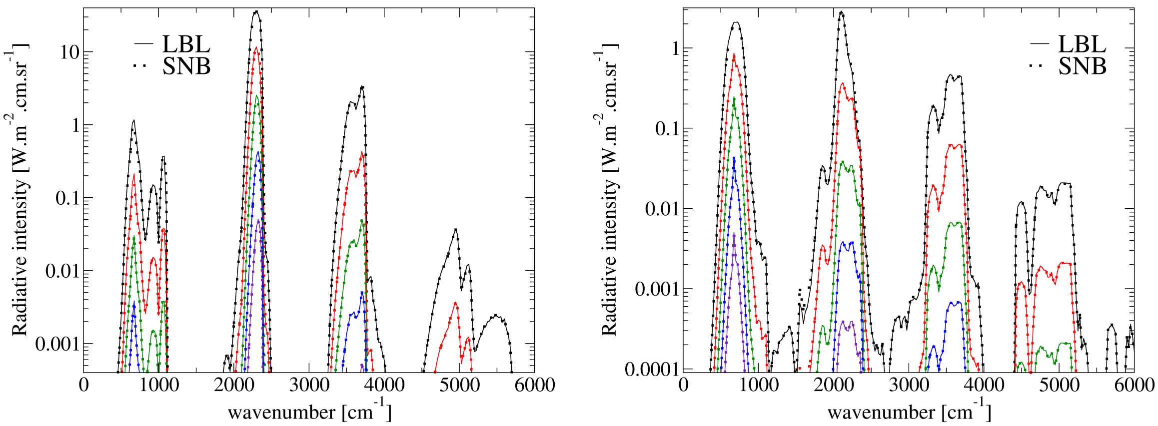

Figure 9: Radiative intensity for a uniform column at $l = 0.1$ m for $x_{\mathrm{CO_2}} = 0.5$, $T = 300$ K, $T_{12} = 1000$ K, $T_3 = 2000$ K (left) and $l = 10$ m for $x_{\mathrm{CO_2}} = 0.5$, $T = 2000$ K, $T_{12} = 1000$ K, $T_3 = 300$ K (right). The pressure is $p = 10000$ Pa (black), $p = 1000$ Pa (red), $p = 100$ Pa (green), $p = 10$ Pa (blue) and $p = 1$ Pa (indigo).

3. Application to radiative transfer

This model aims to be applied in realistic radiative transfer calculations. It must, therefore, give satisfactory results for non-uniform columns. The radiative intensity at the exit of a non-uniform column with N_{col} sub-columns indexed i from the multi-class SNB model is approximated by

$$\overline{I}^{\Delta\sigma}(N^+) = \sum_{j=1}^{N_{class}} \sum_{i=1}^{N_{col}} \overline{\left(\frac{\eta_\sigma}{\kappa_\sigma}\right)_j}^{\Delta\sigma} (T^i, T^i_{12}, T^i_3) \times \\ \left[\overline{\tau_j}^{\Delta\sigma}(i^+ \to N^+) - \overline{\tau_j}^{\Delta\sigma}(i^- \to N^+)\right] \sqrt{\prod_{j' \neq j} \overline{\tau_{j'}}^{\Delta\sigma}(i^+ \to N^+) \prod_{j' \neq j} \overline{\tau_{j'}}^{\Delta\sigma}(i^- \to N^+)}, \quad (30)$$

where $+$ and $-$ represent resp. the inlet and the outlet of the sub-column i. The approximation is valid if each sub-column (i^-, i^+) is optically thin.

The Curtis-Godson (C-G) [32] and Lindquist-Simmons (L-S) [33, 34] approaches are the most commonly used formulations to express the mean transmissivity for non-uniform columns with SNB models. In the Curtis-Godson formulation, it is assumed that the mean transmissivity of a non-uniform column, bounded by abscissae 0 and l, may be expressed similarly to Eq.(19)

$$\overline{\tau}_{CG}^{\Delta\sigma}(0,l) = \exp\left(-\frac{\overline{W}^{CG}}{\delta}(0,l)\right). \tag{31}$$

For the Lorentz broadening regime, the mean black equivalent width is given by

$$\frac{\overline{W}_L^{CG}}{\delta} = \frac{\overline{\beta_L^*}}{\pi}\left(\sqrt{1+\frac{2\pi u^* \overline{k^*}}{\overline{\beta_L^*}}}-1\right), \tag{32}$$

where u^*, $\overline{\beta_L^*}$ and $\overline{k^*}$ are the effective parameters defined as

$$u^* = \int_0^l x_{\mathrm{CO_2}}(s)p(s)\ ds, \tag{33}$$

$$\overline{k^*}u^* = \int_0^l x_{\mathrm{CO_2}}(s)p(s)\bar{k}(s)\ ds, \tag{34}$$

$$\overline{\beta_L^*} = \frac{1}{\overline{k^*}u^*}\int_0^l x_{\mathrm{CO_2}}(s)p(s)\bar{k}(s)2\pi\frac{\overline{\gamma_L}}{\overline{\delta_L}}(s)\ ds. \tag{35}$$

The Curtis-Godson formulation for the Doppler broadening regime is expressed as

$$\frac{\overline{W}_D^{CG}}{\delta} = \overline{\beta_D^*}H_\alpha\left(\frac{u^*\overline{k^*}}{\overline{\beta_D^*}}\right), \tag{36}$$

where $\overline{\beta_D^*}$ can be defined in the classical approach according to

$$\overline{\beta_D^*} = \frac{1}{\overline{k^*}u^*}\int_0^l x_{\mathrm{CO_2}}(s)p(s)\bar{k}(s)\overline{\beta_D}(s)\ ds, \tag{37}$$

and in the formal approach leading to

$$\frac{1}{\overline{\beta_D^*}} = \frac{1}{\overline{k^*}u^*}\int_0^l x_{\mathrm{CO_2}}(s)p(s)\bar{k}(s)\frac{1}{\overline{\beta_D}(s)}\ ds, \tag{38}$$

as provided in [19, 29]. The Lindquist–Simmons approaches provide approximate expressions of the path length derivative of the mean black equivalent width $\overline{W(s,l)}/\delta$ and is defined as follows in [29] for the Doppler and Lorentz broadening regimes

$$-\frac{1}{\delta}\frac{\partial \overline{W}_D^{LS}}{\partial s}(s,\ell) = \overline{k}(s)x_{\mathrm{CO_2}}(s)p(s)y_\alpha\left(\frac{\overline{k^*}(s)u^*(s)}{\overline{\beta_D^*}(s)},\frac{\overline{\beta_D}(s)}{\overline{\beta_D^*}(s)}\right), \tag{39}$$

with

$$y_\alpha(\tilde{x},\tilde{\rho}) = \frac{1}{\sqrt{\pi}}\int_{-\infty}^{+\infty}\frac{e^{-\xi^2}}{\left[1+\tilde{x}\exp\left(-\tilde{\rho}^2\xi^2\right)\right]^{1-\alpha}}\ d\xi, \tag{40}$$

and

$$-\frac{1}{\delta}\frac{\partial \overline{W}_L^{LS}(s,l)}{\partial s} = x_{\mathrm{CO_2}}(s)p(s)\overline{k}(s)y\left[\frac{\pi\overline{k^*}(s)u^*(s)}{\overline{\beta_L^*}(s)},\frac{\overline{\beta_L}(s)}{\overline{\beta_L^*}(s)}\right]. \tag{41}$$

with

$$y(x,\rho) = \frac{2\rho(1+x)+(1+\rho^2)\sqrt{1+2x}}{\sqrt{1+2x}(\rho+\sqrt{1+2x})^2}, \tag{42}$$

As the formulation depends on the parameter $\overline{\beta_D^*}$, there are also classical and formal approaches for the Lindquist-Simmons formulation in the Doppler broadening regime.

To validate the developed SNB model, we consider four cases of non-uniform columns representative of high-altitude plume applications. The first column is a quasi-unidimensional expanding isentropic flow in a conical nozzle of radius $R = 10$ cm at the throat and a cone angle of 15°. The flowing gas is a non-reacting perfect mixture of $\mathrm{N_2}$-$\mathrm{CO_2}$-$\mathrm{H_2O}$ with respective molar fractions

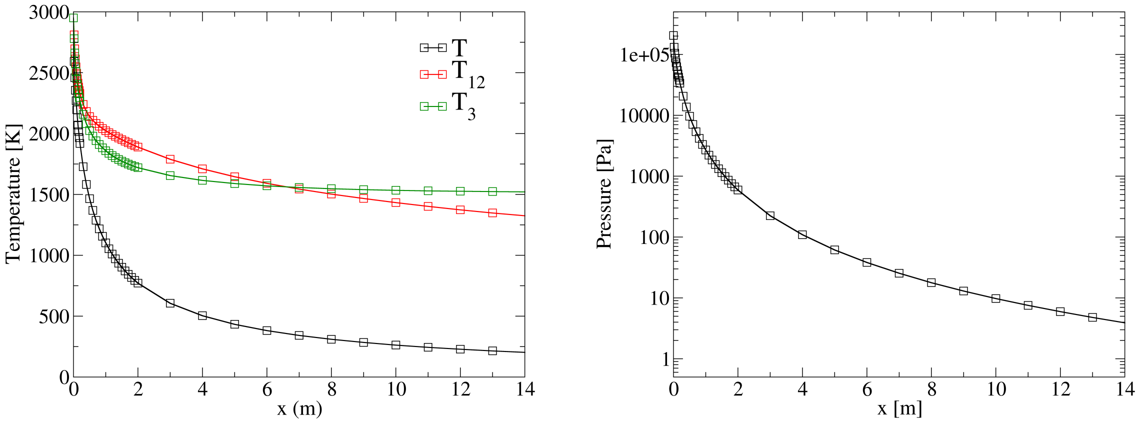

Figure 10: Temperature (left) and pressure (right) profiles of the quasi-unidimensional expanding nozzle flow from [9].

of 70%, 20%, and 10%. The flow conditions at the throat are assumed to be sonic (Mach number=1) with an initial LTE temperature $T_0 = 3000$ K, a mass flow rate of 9 kg.m^{-2}.s^{-1}, leading to an initial velocity $u_0 = 1118$ m.s^{-1}. More details about this case are given in [9]. Fig. 10 shows the pressure and CO_2 temperature profiles during the quasi-unidimensional expansion. The radiative intensity at the exit of the nozzle axis line of sight is computed with the LBL and the SNB approaches and is compared in Fig. 11. We can see that the L-S formal formulation gives the best result in the 15 μm band of CO_2, but the C-G formal approximation is the most accurate one for the 4.3 μm and 2.7 μm bands. To sum up, all the models are accurate for this case and the mean relative errors for the bands presented here are approximately 2%. For this case, the C-G formal approach seems to best agree with the LBL approach if we consider the whole spectrum.

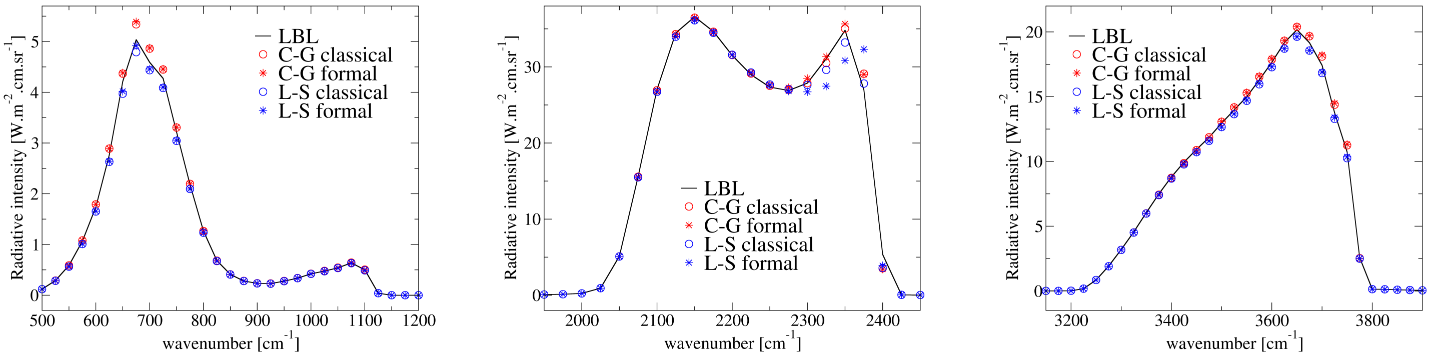

Figure 11: Radiative intensities at the exit of the nozzle axis line of sight in the 15 μm (left), 4.3 μm (middle) and 2.7 μm (right) regions of CO_2 for the quasi-unidimensional expanding flow.

The second and third studied cases are non-uniform columns obtained thanks to a Lagrangian post-processing method applied to LTE simulation of the plume of the solid propellant motor Antares II from the "Bow Shock Ultraviolet2" (BSUV2) experiment [35]. This post-processing method was used on the LTE temperature field of the plume to determine all of the vibrational temperature fields. An exhaustive explanation of this method is presented in [9]. The first column considered is 20 m long, starting from the nozzle exit at $r/2$ from the plume axis of symmetry, where r is the nozzle radius at the nozzle exit and is parallel to the plume axis of symmetry. This case is called hereafter the axial column. The second line of sight called the transverse column, crosses the plume perpendicularly to its axis and intersects this axis at $x = 2$ m away from the nozzle exit. For these two columns, the molar fraction of CO_2 is $x_{CO_2} = 0.0136$. Pressure and temperature distributions along these columns are plotted in Fig.12 and Fig. 14. For the axial column, the L-S classical approach provides the best agreement with the LBL approach

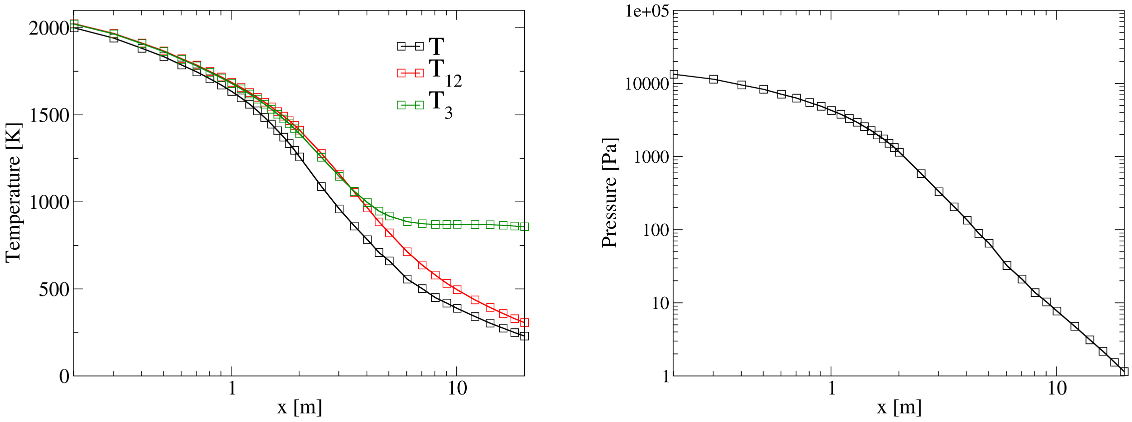

Figure 12: Temperature (left) and pressure (right) profiles of the axial column from [9].

in Fig.13. For the transverse column, the L-S formal approach seems more accurate than the C-G approximation in Fig.15, but the difference is tight.

The last case is a non-uniform column representative of Mars entry conditions. It is a CO_2-N_2 mixture discretized in two uniform columns whose conditions are given in the table 3. The radiative intensity at the exit of the sub-column 2 in the direction $1 \rightarrow 2$ is computed with the SNB model and compared with LBL approach results. Although the HITEMP database might be inaccurate for temperatures around 3500 K, the purpose is to test the SNB model, not the database. It is clear in Fig. 16 that the classical Lindquist-Simmons approach is the most accurate for this case. The 2.7 μm and 15 μm regions are optically thin, so the model degenerates in $\overline{k^*}$ in these bands. We can conclude that the developed nonequilibrium SNB model gives satisfactory results for both strong compression and expansion cases.

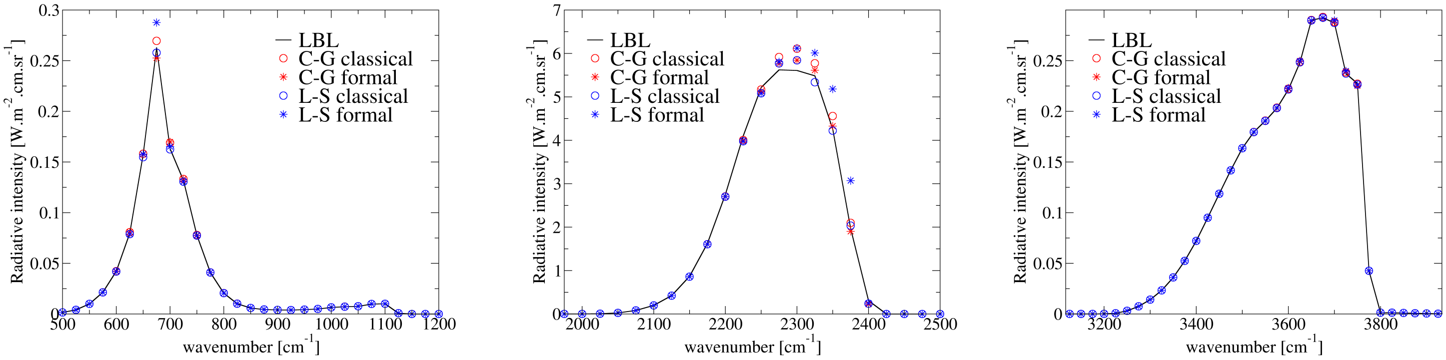

Figure 13: Radiative intensities at the exit of the axial column in the 15 μm (left), 4.3 μm (middle) and 2.7 μm (right) regions of CO_2.

element	p [Pa]	T [K]	T_{12} [K]	T_3 [K]	length [m]	x_{CO_2}
1	1000	3500	1500	700	0.05	0.6
2	500	3000	500	240	0.05	0.6

Table 3: Conditions of the non-uniform column representative of Mars entry conditions

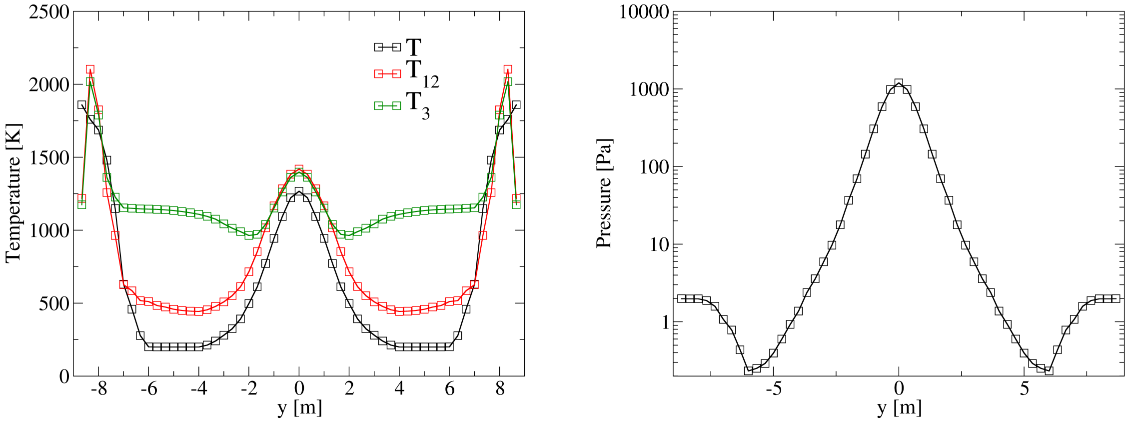

Figure 14: Temperature (left) and pressure (right) profiles of the transverse column from [9].

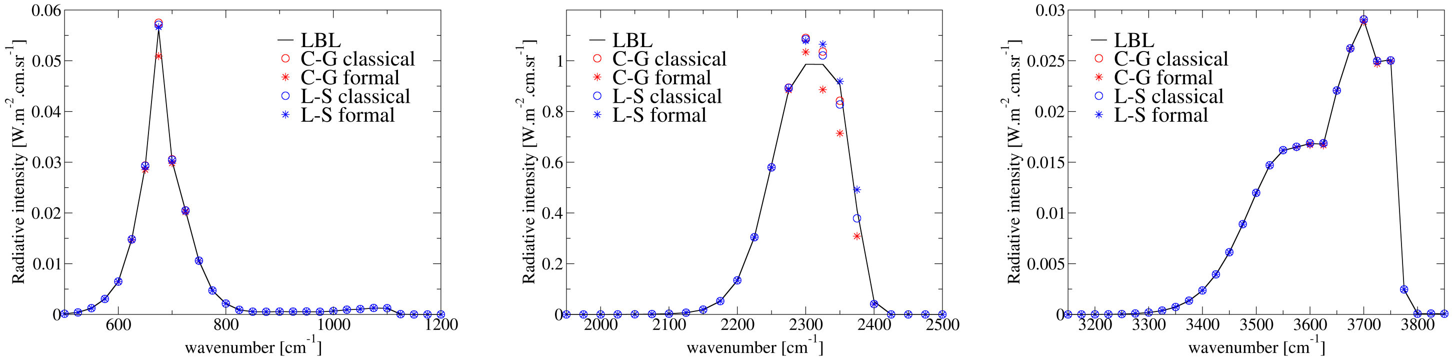

Figure 15: Radiative intensities at the exit of the transverse column in the 15 μm (left), 4.3 μm (middle) and 2.7 μm (right) regions of CO_2.

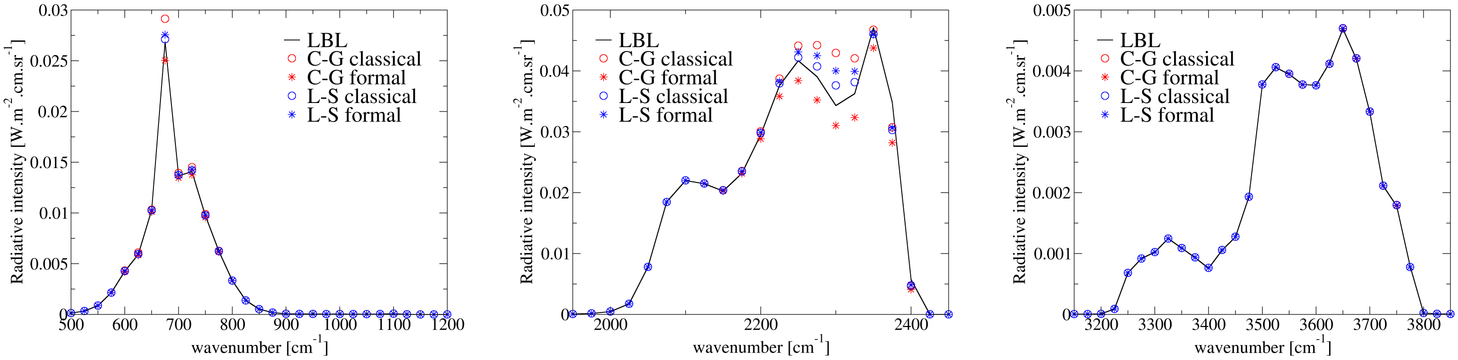

Figure 16: Radiative intensities at the exit of the line of sight in the direction 1 → 2 in the 15 μm (left), 4.3 μm (middle) and 2.7 μm (right) bands of CO_2 for the Mars entry representative conditions.

4. Conclusion

A vibrational nonequilibrium SNB model for CO_2 has been developed and presented in this paper. The calculation of population densities is based on a three-temperature approach (T, T_{12}, T_3) corresponding resp. to the translational-rotational mode, the symmetric stretching and bending mode, and the antisymmetric stretching mode. Since Kirchhoff's law is no longer valid under these conditions, it is necessary to check the decorrelation between $\eta_\sigma/\kappa_\sigma$ and κ_σ beforehand. With these tests, we highlighted that there are correlation issues between $\eta_\sigma/\kappa_\sigma$ and κ_σ in the 4.3 μm and 2.7 μm regions of CO_2 for strong nonequilibrium between the temperatures T_{12} and T_3. This issue is caused by the proximity of transitions whose $\dfrac{\eta_\sigma}{\kappa_\sigma}$ ratio is dominated by the T_{12} and the T_3 temperatures. The proposed solution was to define classes of lines with similar vibrational transitions. SNB model parameters were obtained by adjusting the curves of growth obtained from the LBL approach for Lorentz and Doppler broadening regimes for each line class. The quality of the adjustments was then discussed quantitatively using error statistics. Moreover, the SNB model accuracy was studied for the Voigt broadening regime by comparing the radiative intensity escaping from uniform columns for a wide pressure range in two strong nonequilibrium conditions. This model was also applied for representative cases of high-altitude expanding plumes and Mars entry conditions and showed satisfactory results.

Aknowledgements

The authors acknowledge the financial support of this study from the French Agence de l'Innovation de Défense (AID). This work was granted access to the HPC resources of IDRIS under the allocation 2022-A0102B00209 attributed by GENCI (Grand Equipement National de Calcul Intensif). This work was also performed using HPC resources from the Mésocentre computing center of CentraleSupélec and Ecole Normale Supérieure Paris-Saclay supported by CNRS and Région Île-de-France (http://mesocentre.centralesupelec.fr/).

References

[1] E. V. Kustova, E. A. Nagnibeda, Y. D. Shevelev, N. G. Syzranova, Comparison of different models for non-equilibrium CO_2 flows in a shock layer near a blunt body, Shock waves 111 (2011) 273–287.

[2] J.-M. Lamet, Y. Babou, Ph. Rivière, M.-Y. Perrin, A. Soufiani, Radiative transfer in gases under thermal and chemical nonequilibrium conditions: Application to earth atmospheric re-entry, Journal of Quantitative Spectroscopy and Radiative Transfer 109 (2008) 235–244.

[3] C. K. N. Patel, Continuous-Wave Laser Action on Vibrational-Rotational Transitions of CO_2, Physical Review 136 (1964) 1187–1193.

[4] J. D. Anderson, Gas Dynamic Lasers: An Introduction., Academic press, 1976.

[5] F. S. Simmons, Rocket exhaust plume phenomenology, The Aerospace Press, 2000.

[6] I. Armenise, E. V. Kustova, Mechanisms of Coupled Vibrational Relaxation and Dissociation in Carbon Dioxide, The Journal of Physical Chemistry A 122 (23) (2018) 5107–5120.

[7] V. Kotov, Two-modes approach to the state-to-state vibrational kinetics of CO_2, Journal of Physics B: Atomic, Molecular, and Optical Physics 53 (2020).

[8] T. Kozac, A. Bogaerts, Evaluation of the energy efficiency of CO_2 con-

version in microwave discharges using a reaction kinetics model, Plasma sources science and technology 24 (2015).

[9] Q. Binauld, Ph. Rivière, J.-M. Lamet, L. Tessé, A. Soufiani, CO_2 IR radiation modelling with a multi-temperature approach in flows under vibrational nonequilibrium, Journal of Quantitative Spectroscopy and Radiative Transfer 239 (2019) 106652.

[10] E. V. Kustova, E. A. Nagnibeda, On a correct decription of a multi-temperature dissociating CO_2 flow, Chemical Physics 321 (2006) 293–310.

[11] I. E. Gordon, L. S. Rothman, C. Hill, et al., The HITRAN2016 molecular spectroscopic database, Journal of Quantitative Spectroscopy and Radiative Transfer 203 (2017) 3–69.

[12] L. S. Rothman, I. E. Gordon, R. J. Barber, et al., HITEMP, the high-temperature molecular spectroscopic database, Journal of Quantitative Spectroscopy and Radiative Transfer 111 (2010) 2139–2150.

[13] S. A. Tashkun, V. I. Perevalov, CDSD-4000: High-resolution, high-temperature carbon dioxide spectroscopic databank, Journal of Quantitative Spectroscopy and Radiative Transfer 112 (2011) 1403–1410.

[14] A. Bansal, M. F. Modest, D. A. Levin, Narrow-band *k*-distribution database for atomic radiation in hypersonic nonequilibrium flows, in: HT2009:Proceedings of the ASME summer heat transfer conference, Vol. 1, 2009.

[15] A. Bansal, M. F. Modest, Multiscale Part-Spectrum k-distribution database for atomic radiation in hypersonic nonequilibrium flows, Journal of Heat Transfer-transactions of the ASME 133 (12) (2011).

[16] A. Bansal, M. F. Modest, D. A. Levin, Multiscale k-distribution model for gas mixtures in hypersonic nonequilibrium flows, Journal of Quantitative Spectroscopy and Radiative Transfer 112 (7) (2011) 1213–1221.

[17] A. Sahai, C. O. Johnston, B. Lopez, M. Panesi, Comparative analysis of reduced-order spectral models and grouping strategies for non-equilibrium radiation, Journal of Quantitative Spectroscopy and Radiative Transfer 242 (7) (2020).

[18] L. Pierrot, Ph. Rivière, A. Soufiani, J. Taine, A fictitious-gas-based absorption distribution function global model for radiative transfer in hot gases, Journal of Quantitative Spectroscopy and Radiative Transfer 62 (5) (1999) 609–624.

[19] J.-M. Lamet, Ph. Rivière, M.-Y. Perrin, A. Soufiani, Narrow-band model for nonequilibrium air plasma radiation, Journal of Quantitative Spectroscopy and Radiative Transfer 111 (2010) 87–104.

[20] A. Sahai, C. O. Johnston, B. Lopez, M. Panesi, Flow-radiation coupling in CO_2 hypersonic wakes using reduced-order non-Boltzmann models , Physical Review Fluids 4 (9) (2019).

[21] N. N. Kudriavtsev, S. S. Novikov, Theoretical and experimental investigations of IR radiation transfer in vibrationally nonequilibrated molecu-

lar gas containing CO_2 and CO, International Journal of Heat and Mass Transfer 25 (1982) 1541–1558.

[22] E. I. Vitkin, S. L. Shuralyov, V. V. Tamanovich, Radiation transfer in vibrationally nonequilibrium gases, International Journal of Heat and Mass Transfer 38 (1995) 163–173.

[23] E. I. Vitkin, V. G. Karelin, A. A. Kirillov, A. S. Suprun, J. V. Khadyka, A physico-mathematical model of rocket exhaust plumes, International Journal of Heat and Mass Transfer 40 (1997) 1227–1241.

[24] A. M. Molchanov, L. V. Bykov, D. S. Yanyshev, Calculating thermal radiation of a vibrational nonequilibrium gas flow using the method of k-distribution, Thermophysics and Aeromechanics 24 (2017) 399–419.

[25] G. Herzberg, Molecular spectra and molecular structure. II. Infrared and Raman spectra of polyatomic molecules., Van Nostrand Company, 1956.

[26] A. Chedin, The carbon dioxide molecule: Potential, spectroscopic, and molecular constants from its infrared spectrum, Journal of Molecular Spectroscopy 76 (1979) 430–491.

[27] R. M. Goody, Y. L. Yung, Atmospheric radiation, 2nd Edition, Oxford University Press, 1989.

[28] W. Malkmus, Random Lorentz Band Model with Exponential-Tailed S^{-1} Line-Intensity Distribution Function, Journal of the Optical Society of America 57 (1967) 323–329.

[29] Ph. Rivière, A. Soufiani, Generalized Malkmus line intensity distribution for CO_2 infrared radiation in Doppler broadening regime, Journal of Quantitative Spectroscopy and Radiative Transfer 112 (2011) 475–485.

[30] Ph. Rivière, A. Soufiani, Updated band model parameters for H_2O, CO_2, CH_4 and CO radiation at high temperature, International Journal of Heat and Mass Transfer 55 (2012) 3349–3358.

[31] C. Ludwig, W. Malkmus, J. Reardon, J. Thomson, Handbook of infrared radiation from combustion gases, Technical Report NASA SP-3080, 1973.

[32] S. J. Young, Band model formulation for inhomogeneous optical paths, Journal of Quantitative Spectroscopy and Radiative Transfer 15 (1975) 483–501.

[33] S. J. Young, Nonisothermal band model theory, Journal of Quantitative Spectroscopy and Radiative Transfer 18 (1977) 1–28.

[34] S. J. Young, Addendum to: Band model formulation for inhomogeneous optical paths, Journal of Quantitative Spectroscopy and Radiative Transfer 15 (1975) 1137–1140.

[35] P. W. Erdman, E. Zipf, P. Espy, C. Howlett, D. A. Levin, G. V. Candler, In-situ measurements of UV and VUV radiation from a rocket plume and re-entry bow shock, AIAA Paper (1992) 92–0124.